

Check for updates

# A Robust 3D Cross-Linked Polymer Layer with Controlled Silver Release for Long-Life Anode-Free Lithium Metal Batteries

A-Hyeon Ban, Jin-Ah Roh, Jae-Kyung Choi, Woo Jin Bae, Hyun-Sik Woo, Jongseok Moon, and Dong-Won Kim\*

Anode-free lithium metal batteries (AFLMBs) have been intensively investigated as next-generation energy storage systems because of their high energy density and simplified fabrication processes. However, the poor interfacial compatibility between lithium and the current collector leads to uncontrollable dendrite growth and side reactions, thus hindering their practical application. In this study, a cross-linked polymer protective layer incorporating silver nitrate (Ag-CPL) is proposed, which provides both chemical and mechanical regulation of lithium deposition. The sustained release of Ag+ ions, reduced to form Li-Ag alloys, offers effective nucleation sites that promote uniform lithium plating. The protective layer exhibits a high elastic modulus of 1.2 GPa, effectively suppressing dendritic growth and facilitating uniform lithium-ion transport by promoting desolvation at the interface. As a result, an anode-free pouch cell assembled with a high-loading LiNi<sub>0.88</sub>Co<sub>0.10</sub>Al<sub>0.02</sub>O<sub>2</sub> cathode (22.5 mg cm<sup>-2</sup>) and the Ag-CPL-coated Ni current collector delivered a high initial discharge capacity of 177.7 mAh g<sup>-1</sup> under 80% depth of discharge and exhibited good capacity retention of 80.4% after 200 cycles at 0.5 C and 45 °C. This work demonstrates that the synergistic combination of alloy-guided nucleation and a mechanically robust polymer matrix enables stable interfacial regulation and long-term cycling in AFLMBs.

## 1. Introduction

With the rapid development of mobile electronics and electric vehicles, the demand for rechargeable batteries with high

A.-H. Ban, J.-A. Roh, J.-K. Choi, D.-W. Kim Department of Chemical Engineering Hanyang University Seoul 04763, South Korea E-mail: dongwonkim@hanyang.ac.kr

W. J. Bae, H.-S. Woo, J. Moon SDI R&D Center Samsung SDI Gyeonggi-do 16678, South Korea D.-W. Kim Department of Battery Engineering Hanyang University Seoul 04763, South Korea

The ORCID identification number(s) for the author(s) of this article can be found under https://doi.org/10.1002/adfm.202518139

DOI: 10.1002/adfm.202518139

energy density has been steadily increasing.[1-3] Lithium metal, possessing an extremely high theoretical capacity (3,860 mAh g<sup>-1</sup>) and the lowest redox potential (-3.04 V vs. SHE), is considered a promising alternative to conventional graphite-based anodes for achieving high energy density.[4-6] Among the various configurations of lithium metal batteries, anode-free lithium metal batteries (AFLMBs) have recently emerged as promising next-generation energy storage systems due to their high energy density, low cost, simplified fabrication process, and improved safety.[7,8] By eliminating excess lithium on the anode side, AFLMBs can significantly reduce overall battery weight while achieving energy densities exceeding 400 Wh kg<sup>-1</sup> at the cell level.<sup>[9]</sup> Despite these advantages, the practical application of AFLMBs is mainly hindered by limited cycle life. The thermodynamic mismatch and high nucleation energy barrier between Li and the current collector, such as Cu foils, induce irregular lithium nucleation.[10] Furthermore, the

non-uniformity leads to uncontrolled lithium dendrite growth, repeated regeneration of the solid-electrolyte interphase (SEI), electrolyte depletion, and irreversible lithium loss. [11] The formation of Li dendrites in lithium metal batteries has been explained by two representative models: the Chazalviel model, which attributes dendrite growth to ion depletion and transport limitations, and the Monroe–Newman model, which considers mechanical instability at the Li–electrolyte interface as the primary driving force. [12–13] These perspectives emphasize the importance of both stable lithium-ion transport and a mechanically robust SEI layer to ensure uniform lithium deposition and long-term cycling.

Based on this understanding, various strategies have been proposed to regulate the lithium–electrolyte interface, including electrolyte optimization,<sup>[14–16]</sup> separator modification,<sup>[17,18]</sup> designing 3D electrode structures,<sup>[19,20]</sup> and applying artificial SEI layers.<sup>[21–23]</sup> Among these strategies, the construction of artificial SEI layers has attracted significant attention due to their tunable composition, structural stability, and compatibility with scalable fabrication processes.<sup>[24–27]</sup> However, most approaches

www.afm-journal.de

1616328.2025, 42, Downloaded from https://advanced.onlinelibrary.wiley.com/doi/10.1002/atmf.202518139 by Hanyang University. Wiley Online Library on [17/10/2025]. See the Terms and Conditions (https://onlinelibrary.wiley.com/erms-and-conditions) on Wiley Online Library for rules of use; OA articles are governed by the applicable Creative Commons to 117/10/2025. See the Terms and Conditions (https://onlinelibrary.wiley.com/erms-and-conditions) on Wiley Online Library for rules of use; OA articles are governed by the applicable Creative Commons to 117/10/2025.

address either ionic transport or interfacial stability, but not both. For example, inorganic-based protective layers offer high ionic conductivity but are often brittle and prone to fracture due to volume changes. In contrast, polymer-based layers provide flexibility and interfacial adhesion but suffer from mechanical degradation caused by swelling in liquid electrolytes.<sup>[28,29]</sup> Recently, silver nitrate (AgNO<sub>3</sub>) has been extensively studied as a dualfunctional additive.[30] It not only supplies NO<sub>3</sub> ions but also releases highly lithiophilic Ag+ ions. Silver exhibits high electrical conductivity and a strong affinity for lithium, effectively reducing the nucleation overpotential and promoting uniform lithium plating.[31,32] For instance, Ag-coated lithium metal electrodes have demonstrated a uniform lithium-ion flux, suppressing dendritic lithium growth.<sup>[33]</sup> Upon initial charging, Ag<sup>+</sup> ions are electrochemically reduced to form metallic Ag and Li-Ag alloys at the electrode surface, providing thermodynamically favorable nucleation sites that promote uniform lithium plating. In addition, in situ reduction of NO<sub>3</sub><sup>-</sup> leads to the formation of Li<sub>3</sub>N, a highly Li<sup>+</sup>-conductive material that effectively stabilizes lithium deposition.[34,35] However, the solubility limitations of AgNO<sub>3</sub> in carbonate-based electrolytes remain a critical technical challenge, necessitating a suitable host material to enable controlled, sustained release.[36,37]

Building upon these insights, we designed an AgNO<sub>3</sub> incorporated cross-linked polymer protective layer (Ag-CPL) with a high Li<sup>+</sup> transference number and superior mechanical strength. The Ag-CPL offers several versatile advantages: i) Robust cross-linked polymer network: The network prevents direct contact between the liquid electrolyte and metallic Li, suppressing undesired side reactions and physically inhibiting lithium dendrite growth. ii) Facilitated Li<sup>+</sup> desolvation and transport: The polymer matrix coordinates with lithium-ions, ensuring a uniform Li<sup>+</sup> flux, which promotes homogeneous lithium deposition on the substrate. iii) Sustained release of Ag+ and NO3-: AgNO3 dispersed within the polymer matrix gradually dissolves into the electrolyte during cycling, continuously maintaining the concentration of Ag+ and NO<sub>3</sub><sup>-</sup> at the anode surface. The released Ag<sup>+</sup> ions are reduced to form highly conductive Li-Ag alloys, which act as nucleation sites to lower the nucleation overpotential and promote uniform lithium plating. Concurrently, NO<sub>3</sub> - ions decompose to form an inorganic-rich SEI (mainly Li<sub>3</sub>N and LiN<sub>v</sub>O<sub>v</sub>), enhancing ionic conductivity and further stabilizing the electrode-electrolyte interface.

Leveraging these attributes, an anode-free pouch cell (Ni/LiNi $_{0.88}$ Co $_{0.10}$ Al $_{0.02}$ O $_2$  cell, active mass loading: 22.5 mg cm $^{-2}$ ) incorporating the Ag-CPL exhibited a superior capacity retention of 80.4% after 200 cycles. Moreover, the introduction of Ag-CPL significantly improved lithium deposition uniformity, reduced nucleation overpotential from 64 to 21 mV, and increased the Li $^+$  transference number from 0.29 to 0.41, thus effectively mitigating dendritic lithium growth and suppressing electrolyte depletion. Overall, this work presents a feasible and practical strategy to substantially enhance the efficiency, cycling stability, and cycle life of AFLMBs.

## 2. Results and Discussion

A schematic illustration of the Ag-CPL fabrication process is presented in Figure S1 (Supporting information), and the detailed

procedure is provided in the Experimental Section. Figure 1a,b shows an FE-SEM image of Ag-CPL coated on Ni foil (Ag-CPL-Ni) and the corresponding EDS elemental mapping images, respectively. The detected C and F elements originate from the crosslinked polymeric layer. As revealed in SEM-EDS mapping images of N and Ag elements, the AgNO3 nanoparticles are uniformly distributed and embedded in polymer networks. The chemical state of Ag species in Ag-CPL was characterized by XPS and XRD analyses. As shown in Figure 1c, the deconvoluted XPS spectrum of Ag-CPL exhibits peaks corresponding to AgNO<sub>3</sub>, metallic Ag, and Ag<sub>2</sub>O. As expected, the characteristic peaks corresponding to AgNO<sub>3</sub> are observed at 368.8 and 374.8 eV. Additional peaks at 368.3 and 374.3 eV confirm the presence of trace amounts of metallic Ag nanoparticles, which were inevitably formed during the fabrication process through a simple replacement reaction  $(Ni + 2Ag^{+} = Ni^{2+} + 2Ag)$ . The XRD pattern of Ag-CPL-Ni (Figure 1d) shows three additional peaks besides the Ni peaks. The peak at 38.1° corresponds to the (111) crystal plane of facecentered cubic Ag, with peak splitting attributed to the Cu K<sub>a1</sub> and K<sub>a2</sub> wavelength difference.<sup>[39]</sup> These results confirm that Ag-CPL-Ni contains two sources of Ag: (i) a trace amount of predeposited Ag nanoparticles formed during its preparation, and (ii) the sustained release of Ag+ ions from AgNO3 during battery cycling. The Ag-CPL was synthesized by radical polymerization of three acrylate monomers - poly(ethylene glycol) diacrylate (PEGDA), dipentaerythritol hexaacrylate (DPHA), and perfluoropolyether-urethane acrylate (PFPE-UA) - whose chemical structures are shown in Figure S2a-c (Supporting information). FT-IR analysis was performed to confirm the cross-linking reaction of these monomers (Figure 1e). All the spectra exhibit a characteristic peak at 1723 cm<sup>-1</sup>, corresponding to the C=O stretching vibration of the acrylate groups. The peak at 1633 cm<sup>-1</sup> observed in the PEGDA, DPHA, and PFPE-UA spectra corresponds to the C=C stretching vibration.<sup>[40]</sup> The disappearance of the C=C peak in the FT-IR spectrum of Ag-CPL after thermal cross-linking of PEGDA, DPHA, and PFPE-UA confirms the complete radical polymerization of the C=C double bonds and the formation of cross-linked polymer networks. The extent of thermal cross-linking reaction in Ag-CPL was further evaluated by <sup>1</sup>H NMR spectroscopy, as previously reported. <sup>[40,41]</sup> The <sup>1</sup>H NMR spectra of the cross-linking agents are presented in Figure S2d,e (Supporting information). Characteristic peaks at 6.3, 6.1, and 5.8 ppm correspond to protons A, B, and C in the acrylate groups. Figure 1f shows the 1H NMR spectra of the precursor solution and Ag-CPL. For quantitative analysis, a small amount of the precursor solution (or Ag-CPL) was transferred into NMR tubes with 1 wt.% p-Xylene added as an internal standard. After thermal curing for 1.5 h, the peak intensities of protons A, B, and C significantly decreased, indicating a successful cross-linking reaction. Table S1 (Supporting information) summarizes the normalized <sup>1</sup>H peak intensities and calculated conversions. These results confirm a high polymerization conversion of 99.8%, which is consistent with the FT-IR analysis.

Owing to its cross-linked network structure, Ag-CPL is expected to exhibit superior mechanical strength compared to conventional linear polymer-based protective layers. To validate this, the mechanical strength of Ag-CPL was evaluated using nanoindentation, and the corresponding load–depth curve is presented in Figure S3 (Supporting information). As the

16163028, 2025. 42, Downloaded from https://advanced.onlinelibrary.wiley.com/doi/10.1002/adfm.202518139 by Hanyang University, Wiley Online Library on [17/10.2025]. See the Terms and Conditions (https://onlinelibrary.wiley.com/erms

conditions) on Wiley Online Library for rules of use; OA articles are governed by the applicable Creative Commons

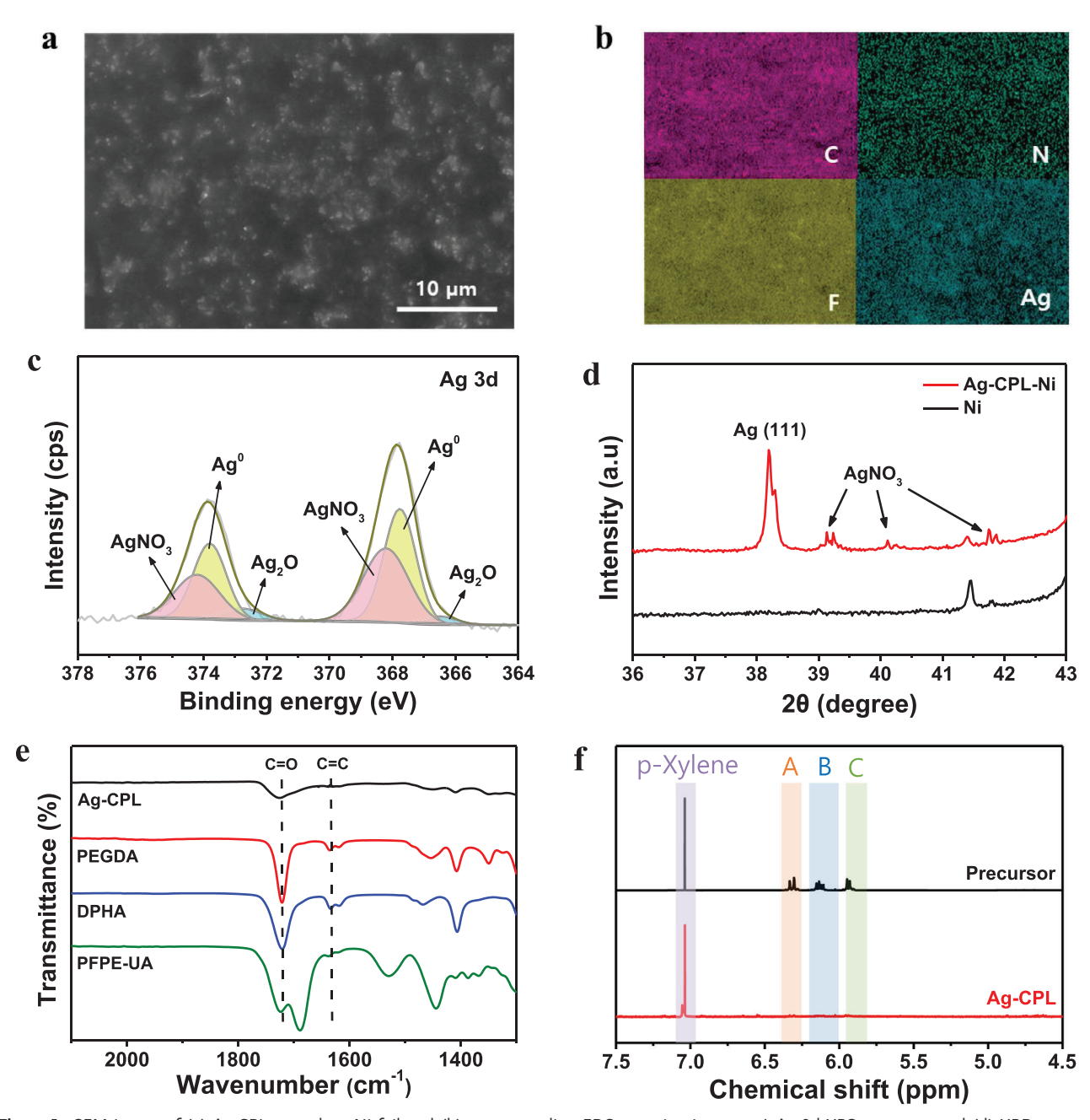


**Figure 1.** SEM image of (a) Ag-CPL coated on Ni foil and (b) corresponding EDS mapping images. c) Ag 3d XPS spectrum and (d) XRD pattern of Ag-CPL. e) FT-IR spectra of Ag-CPL, PEGDA, DPHA, and PFPE-UA. f) <sup>1</sup>H NMR spectra of precursor and Ag-CPL.

applied load increased, the surface of Ag-CPL was gradually penetrated by the nanoindenter tip, and the resulting penetration depth was recorded. It is well-established that a higher crosslink density enhances mechanical properties, including elastic modulus and hardness.<sup>[42]</sup> The Ag-CPL exhibited an elastic modulus of 1.24 GPa (Table S2, Supporting information), significantly higher than that of commonly used linear polymer protective layers (<1.0 MPa).<sup>[43]</sup> Such excellent mechanical properties can be mainly attributed to the copolymerization of PFPE-UA and DPHA, which contain four and six functional groups,

respectively, contributing to a highly cross-linked network structure. These results suggest that Ag-CPL can effectively suppress dendritic lithium growth through its enhanced mechanical robustness.

The solubility of  $AgNO_3$  in the liquid electrolyte was determined using ICP-MS. The concentration of  $Ag^+$  ions reached the solubility limit of  $\approx 550$  ppm within 3 h of immersing AgCPL in the electrolyte and remained at the same level thereafter (**Figure 2a**). During the charging process, the eluted  $Ag^+$  ions are likely to be preferentially converted to Li-Ag alloy on the

16163028, 2025, 42, Downloaded from https://adv

onlinelibrary.wiley.com/doi/10.1002/adfm.202518139 by Hanyang University, Wiley Online Library on [17/10/2025]. See the Terms and Conditions (https://onlinelibrary.wiley.com/

of use; OA articles are governed by the applicable Creative Commons

www.afm-journal.de

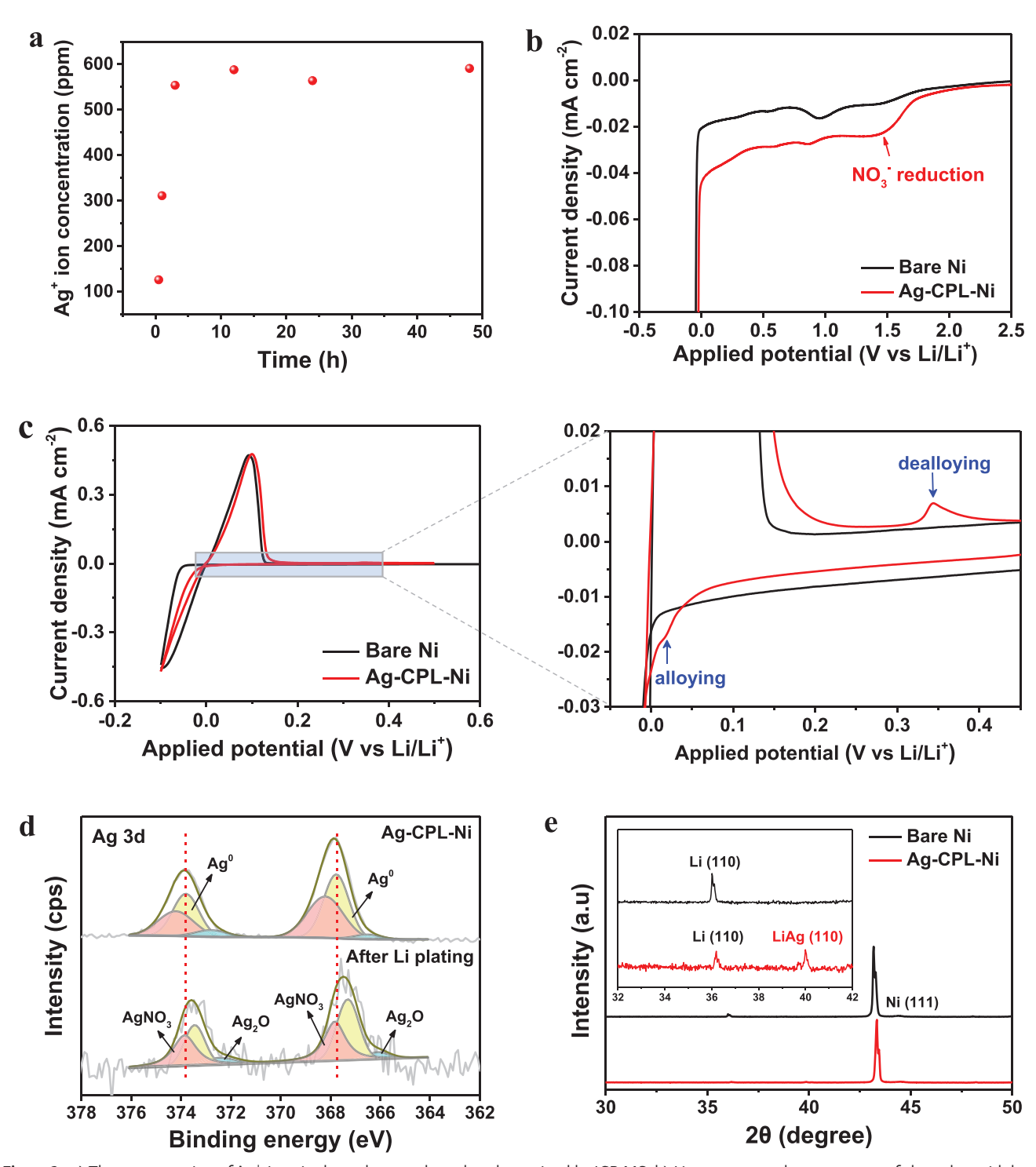


Figure 2. a) The concentration of  $Ag^+$  ions in the carbonate electrolyte determined by ICP-MS. b) Linear sweep voltammograms of electrolyte with bare Ni and Ag-CPL-Ni. c) Cyclic voltammograms of the bare Ni and Ag-CPL-Ni in the carbonate electrolyte at a scan rate of 1.0 mVs<sup>-1</sup>. d) Ag 3d XPS spectra of Ag-CPL-Ni electrodes before (top) and after (bottom) lithium plating. e) XRD patterns of lithium plated on bare Ni and Ag-CPL-Ni.

current collector, which serves as lithiophilic nucleation sites that promote uniform lithium deposition.<sup>[44]</sup> The electrochemical stability of the Ag-CPL was evaluated by linear sweep voltammetry (LSV), as shown in Figure 2b. Since the LSV was conducted using a carbonate-based electrolyte, the cell with bare Ni

exhibited typical reductive decomposition peaks corresponding to the salts and solvents. In contrast, the cell with Ag-CPL-Ni showed an additional peak at 1.7 V, which is attributed to the reduction of NO<sub>3</sub><sup>-</sup> originating from AgNO<sub>3</sub> within the Ag-CPL. NO<sub>3</sub><sup>-</sup> anions have been reported to modify the SEI layer by

www.advancedsciencenews.com



www.afm-journal.de

forming Li<sub>3</sub>N-rich species, thereby enhancing lithium-ion conductivity and improving the cyclability of the lithium metal anode. Consequently, the AgNO<sub>3</sub> not only promotes uniform lithium deposition but also regulates the composition of the SEI layer. To further investigate the lithium deposition behavior, cyclic voltammetry (CV) was conducted during the initial plating/stripping processes on bare Ni and Ag-CPL-Ni electrodes, and the resulting cyclic voltammograms are shown in Figure 2c. The CV curves of both cells exhibited distinct peaks between -0.1and 0.1 V, corresponding to the typical stripping and plating of metallic lithium on the current collector. Notably, the Ag-CPL-Ni cell displayed two additional peaks at 0.02 and 0.34 V, which are attributed to Li-Ag alloying and dealloying reactions. [45] The formation of a Li-Ag alloy was further confirmed by XPS and XRD analyses. To investigate the nucleation and initial growth of lithium, 0.1 mAh cm<sup>-2</sup> of lithium was deposited onto bare Ni and Ag-CPL-Ni, respectively. The upper Ag 3d spectrum in Figure 2d represents the as-prepared Ag-CPL-Ni prior to lithium deposition, exhibiting two characteristic peaks corresponding to metallic Ag. After lithium plating, these peaks shifted from 368.3 and 374.3 eV to 361.5 and 367.5 eV, respectively, indicating a decrease in binding energy due to strong Li-Ag interactions. This shift confirms the formation of a Li-Ag alloy. [46] XRD analysis further supports this finding (Figure 2e). XRD patterns of bare Ni and Ag-CPL-Ni exhibit Ni(111) peak at 44.6° and Li(110) peak at 36.2°. The Ag-CPL-Ni exhibits an additional peak at 40.2°, corresponding to the (110) diffraction peak of the Li-Ag alloy. These results confirm that Ag-CPL contains two sources of Ag, both of which are converted into Li-Ag alloys during the initial plating, indicating that the predominant mechanism for reducing the nucleation overpotential is the formation of Li-Ag alloys. The formation of a highly conductive and lithiophilic Li-Ag can reduce nucleation overpotential, thereby suppressing dendritic lithium growth and promoting uniform lithium deposition.

To investigate the influence of Ag-CPL on the desolvation behavior of Li<sup>+</sup> ions at the bulk electrolyte/lithium interface, FT-IR and Raman analyses were conducted on liquid electrolyte with and without Ag-CPL. Figure 3a presents the deconvoluted FT-IR spectra of the C=O stretching vibrations from the diethyl carbonate (DEC) solvent in the electrolyte. The peaks at 1744 and 1717 cm<sup>-1</sup> correspond to free DEC and solvated DEC, respectively. Upon the introduction of Ag-CPL, two additional peaks appeared at 1725 and 1700 cm<sup>-1</sup>, which were absent in the electrolyte without Ag-CPL. These new peaks originate from the acrylate groups within Ag-CPL; specifically, the peak at 1725 cm<sup>-1</sup> is assigned to free acrylate groups, while the peak at 1700 cm<sup>-1</sup> corresponds to acrylate groups coordinated with Li<sup>+</sup>. These ion-dipole interactions are believed to facilitate Li+ dissociation and modulate the lithium-ion solvation structure. Further evidence was obtained from Raman spectroscopy. As shown in Figure 3b, the Raman peaks between 840 and 940 cm<sup>-1</sup> were deconvoluted into five distinct peaks, corresponding to free and Li<sup>+</sup>-coordinated solvent molecules. Notably, the intensity of the peak at 922 cm<sup>-1</sup>, attributed to coordinated solvent molecules, significantly decreased in the presence of Ag-CPL compared to the electrolyte without Ag-CPL. Density functional theory (DFT) calculation was conducted to obtain molecular-level insights into these spectroscopic results. For computational feasibility, the calculations were performed on representative monomer units or fragment structures

Adv. Funct. Mater. 2025, 35, e18139

that included the relevant functional groups. Figure S4 (Supporting information) presents the calculated binding energies of Li<sup>+</sup>-solvent and Li<sup>+</sup>-monomer pairs. The DFT results indicate that PEGDA( $-CH_2CH_2O-$ ) - Li<sup>+</sup>(-3.16 eV) and DPHA(C=O) -Li<sup>+</sup>(-2.19 eV) exhibit stronger binding energies than common carbonate solvents, such as FEC (C=O) - Li+ (-2.01 eV) and DEC (C=O) –  $Li^+$  (-2.04 eV). This suggests that these functional groups can preferentially coordinate Li+ and facilitate desolvation at the electrode interface. In contrast, PFPE-UA does not provide effective Li<sup>+</sup> ion coordination; instead, the fluorine-rich environment weakly stabilizes Li+ ions through electrostatic interactions (-1.18 eV), consistent with previous reports on fluorinated electrolytes. [47,48] Such a weak stabilization does not hinder Li<sup>+</sup> dynamics but can contribute to a complementary conduction environment. These computational findings corroborate the FT-IR and Raman results, which demonstrate decreased Li+solvent coordination in the presence of Ag-CPL. The transport of lithium-ions in electrolytes with and without Ag-CPL was investigated by measuring the Li+ transference numbers, as shown in Figure 3c,d. The electrolyte with Ag-CPL exhibited higher Li<sup>+</sup> transference number ( $t_{Ii^+} = 0.41$ ) compared to that without Ag-CPL ( $t_{Lit}$  = 0.29). This enhancement is attributed to the polymer matrix in the Ag-CPL, which promotes Li<sup>+</sup> desolvation and facilitates faster lithium-ion migration, as confirmed by FT-IR and Raman analyses. Consequently, the higher Li<sup>+</sup> transference number reduces interfacial polarization and supports uniform lithium deposition at the anode. Additionally, to further elucidate the effect of Ag-CPL on lithium electrodeposition, the exchange current density (in) was determined from the Tafel plots shown in Figure 3e. Ag-CPL-Ni exhibited a higher exchange current density (0.48 mA cm<sup>-2</sup>) compared to bare Ni (0.28 mA cm<sup>-2</sup>), indicating enhanced interfacial charge transfer facilitated by the presence of the Ag-CPL at the electrode–electrolyte interface.<sup>[49]</sup> These combined results suggest, as schematically illustrated in Figure 3f, that Ag-CPL induces ion-dipole interactions that weaken Li<sup>+</sup>-solvent coordination, thereby promoting Li<sup>+</sup> desolvation and contributing to uniform lithium deposition.

To evaluate the electrochemical performance of Ag-CPL as a protective layer, Li/Ni half-cells were assembled using bare Ni and Ag-CPL-Ni electrodes and tested at a current density of 1 mA cm<sup>-2</sup>. Figure 4a presents the voltage-capacity curves during the initial lithium electrodeposition on each electrode. The nucleation overpotential was only 21 mV for the Ag-CPL-Ni electrode,  $\approx$ 3 times lower than that of bare Ni (64 mV). This result indicates that Ag-CPL effectively reduces the nucleation energy barrier by providing abundant lithium nucleation sites on the electrode surface.<sup>[50]</sup> The Coulombic efficiency (CE) is a critical parameter that reflects lithium loss per cycle and is directly correlated with battery cycle life, particularly in AFLMBs, where no excess lithium source is available. As shown in Figure 4b, the cell with bare Ni exhibited an average CE of ≈89%, with pronounced fluctuations appearing after ≈50 cycles. Furthermore, the CE of the bare Ni electrode declined sharply. This instability and abrupt drop are attributed to uncontrolled SEI formation and dendritic lithium growth, which result in electrolyte depletion and irreversible lithium consumption. In contrast, the Li/Ag-CPL-Ni cell demonstrated outstanding cycling stability, maintaining a significantly higher CE of  $\approx$ 98% over 100 cycles. Figure 4c,d shows the voltage profiles of cells with bare Ni and Ag-CPL-Ni electrodes at

16163028, 2023, 42, Downloaded from https://advanced.onlinelibrary.wiley.com/doi/10.1002/adfm.202518139 by Hanyang University, Wiley Online Library on [17/102025]. See the Terms and Conditions (https://onlinelibrary.wiley.

conditions) on Wiley Online Library for rules of use; OA articles are governed by the applicable Creative Commons

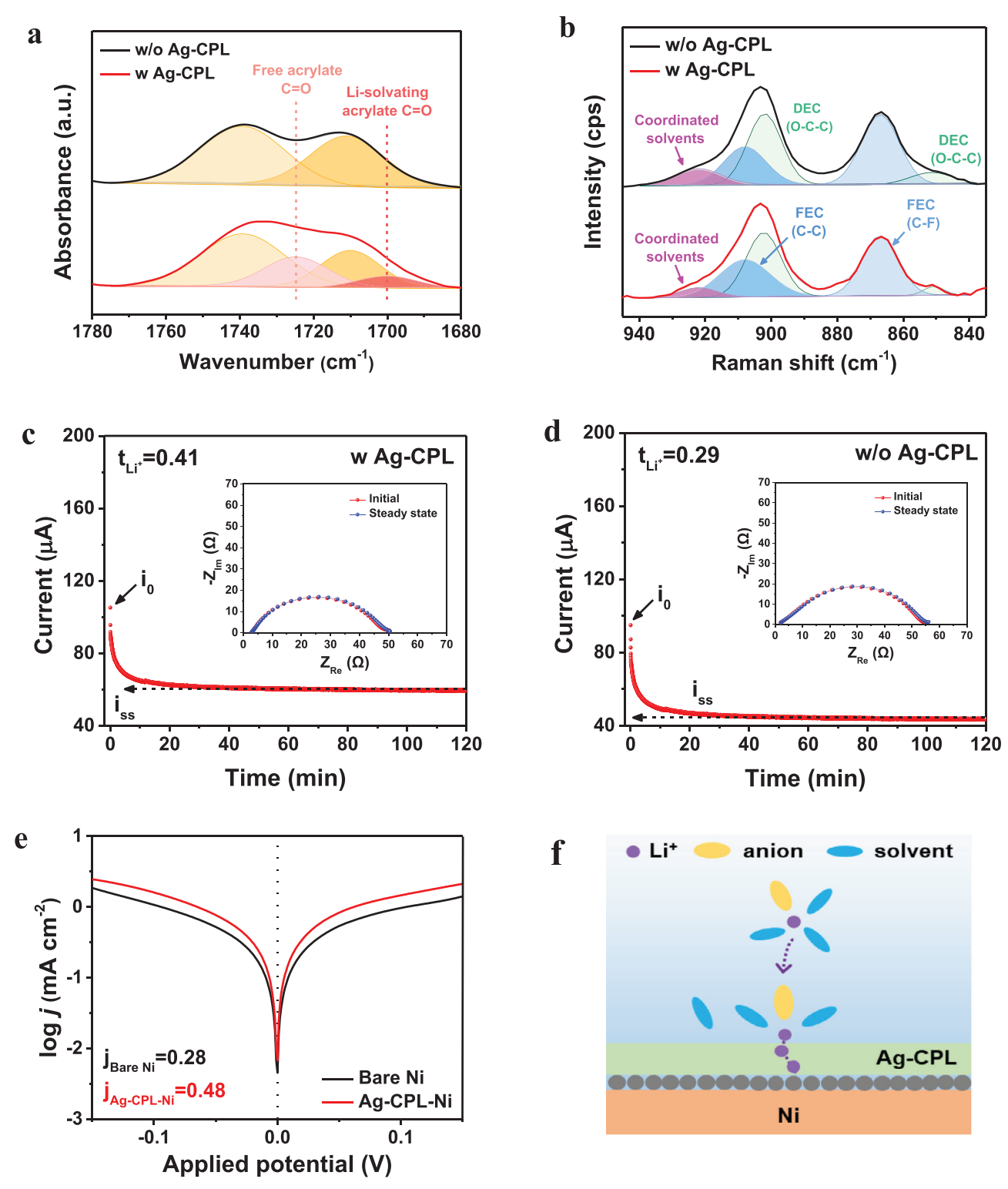


Figure 3. a) FT-IR spectra and corresponding fitting results of the liquid electrolyte with and without Ag-CPL. b) Raman spectra of the solvents in the liquid electrolyte with and without Ag-CPL. c,d) Chronoamperometry curve of a symmetric Li/Li cell under a polarization voltage of 10 mV. The inset shows Nyquist plots of the symmetric Li/Li cells (c) with Ag-CPL and (d) without Ag-CPL before and after polarization. e) Tafel plots of Ni/Ni cells using bare Ni and Ag-CPL-Ni in the liquid electrolyte. f) Schematic illustration of the solvation environment and lithium electrodeposition on Ag-CPL-Ni.

16163028, 2025. 42, Downloaded from https://advanced.onlinelibrary.wiley.com/doi/10.1002/adfm.202518139 by Hanyang University, Wiley Online Library on [17/10.2025]. See the Terms and Conditions (https://onlinelibrary.wiley.com/

nditions) on Wiley Online Library for rules of use; OA articles are governed by the applicable Creative Commons

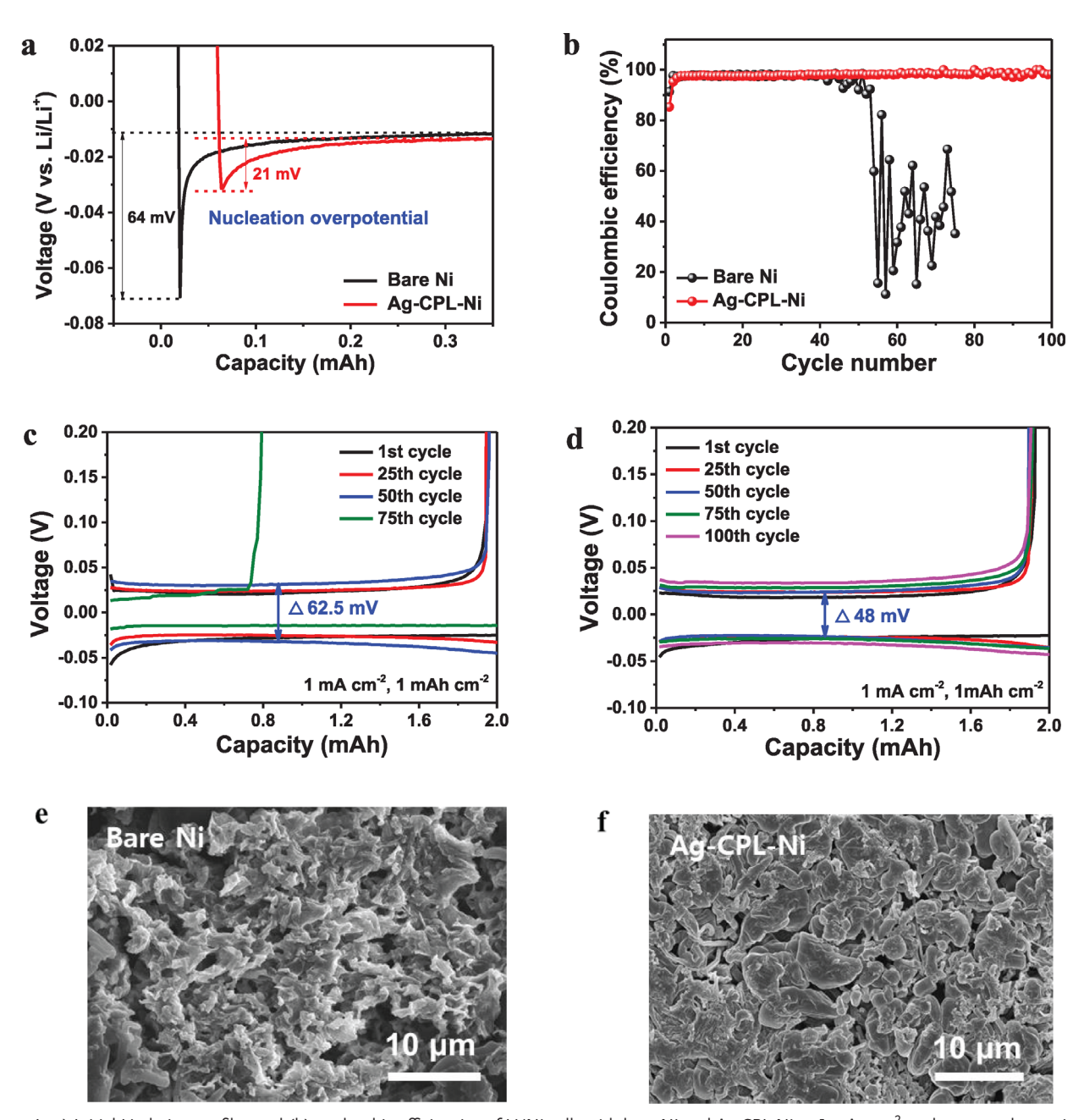


Figure 4. a) Initial Li plating profiles and (b) coulombic efficiencies of Li/Ni cells with bare Ni and Ag-CPL-Ni at 1 mA cm<sup>-2</sup> under an areal capacity of 1 mAh cm<sup>-2</sup>. Voltage profiles of Li/Ni cells with (c) bare Ni and (d) Ag-CPL-Ni electrodes. SEM images of lithium deposited on (e) bare Ni after 75 cycles and (f) Ag-CPL-Ni after 100 cycles.

different cycles. After 50 cycles, the cell with bare Ni exhibited a higher voltage polarization of 62.5 mV, whereas the Ag-CPL-Ni electrode maintained a lower and more stable voltage polarization of 48 mV, demonstrating its capability for stable lithium plating/stripping performance. To further examine Li<sup>+</sup> transport behavior, we conducted galvanostatic intermittent titration technique (GITT) measurements using symmetric cells composed of Li-plated bare Ni and Ag-CPL-Ni electrodes. As presented in Figure S5 (Supporting information), the Ag-CPL cell consistently exhibited lower overpotential during plating and stripping compared to the bare Ni cell, reflecting reduced interfacial concen-

tration gradients and more uniform lithium deposition kinetics. Morphological analysis further supports these electrochemical observations. After 75 cycles, lithium deposition on bare Ni exhibited a dendritic, mossy, and uneven structure (Figure 4e). In contrast, lithium deposits on Ag-CPL-Ni after 100 cycles displayed dendrite-free, uniform, and pebble-like morphologies (Figure 4f), which are attributed to the high nucleation density and uniform nucleation facilitated by Ag-CPL.

To evaluate the effect of Ag-CPL on the cycling performance, pouch-type anode-free full cells were assembled using Ni-based anodes (bare Ni and Ag-CPL-Ni) paired with a high-loading NCA

www.afm-journal.de

16162928, 2025, 42, Downloaded from https://advanced.onlinelibrary.wiley.com/doi/10.1002/atmf.202518139 by Hanyang University, Wiley Online Library on [17102025]. See the Terms and Conditions (https://onlinelibrary.wiley.com/erms-and-conditions) on Wiley Online Library or rules of use; OA articles are governed by the applicable Creative Commons to

cathode (active materials: 22.5 mg cm<sup>-2</sup>) and carbonate-based electrolyte. The AgNO3 content was systematically varied during Ag-CPL fabrication, and the resulting full-cell performance was evaluated. As shown in Figure S6 (Supporting information), the pure CPL (0 wt.% AgNO<sub>3</sub>) exhibited inferior cycling stability compared with Ag-CPL incorporating AgNO3, indicating that the incorporation of AgNO3 enhances cycling stability beyond that provided by the polymer matrix alone. The cycling stability improved with increasing AgNO<sub>3</sub> content up to 37 wt.%, whereas further increases led to performance degradation. This decline at higher AgNO3 content can be attributed to excessive Ag+, which induces irregular Ag deposition and uneven lithium plating/stripping. Therefore, 37 wt.% AgNO<sub>3</sub> was identified as the optimal composition and employed for cell fabrication. Prior to the long-term cycling test, the Ni/NCA cells were pre-cycled at 0.1 C rate. Figure S7 (Supporting information) shows the voltage profiles of the cells under two depth of discharge (DoD) conditions: 2.8-4.3 V (100% DoD) and 3.6-4.3 V (80% DoD). The cell with bare Ni delivered specific capacities of 215.3 mAh g<sup>-1</sup> (areal capacity: 4.84 mAh cm<sup>-2</sup>) under 100% DoD and 174.0 mAh g<sup>-1</sup> under 80% DoD. In comparison, the Ag-CPL-Ni cell exhibited slightly higher capacities of 218.2 mAh g<sup>-1</sup> (areal capacity: 4.90 mAh cm<sup>-2</sup>) for 100% DoD and 177.7 mAh g<sup>-1</sup> for 80% DoD. Figure 5a,b depict the voltage profiles of Ni/NCA full cells assembled with bare Ni and Ag-CPL-Ni, respectively. During the first cycle at 0.5 C rate, the cell with Ag-CPL-Ni delivered a slightly higher discharge capacity (167.7 mAh g<sup>-1</sup>) than the cell with bare Ni (162.8 mAh g<sup>-1</sup>). While the discharge capacity of the bare Ni/NCA cell sharply declined to 13.1 mAh g-1 after 200 cycles, the Ag-CPL-Ni/NCA cell maintained a high capacity of 134.9 mAh g<sup>-1</sup> with less capacity fading. The corresponding cycling performance of the cells with different anodes is shown in Figure 5c. The Ag-CPL-Ni/NCA cell retained 80.4% of its initial capacity after 200 cycles, whereas the bare Ni/NCA cell exhibited rapid capacity fading, retaining only 8.0%. The severe capacity loss in the bare Ni cell is attributed to uncontrolled side reactions between the lithium anode and the electrolyte, induced by the formation of dendritic lithium. These results demonstrate that the use of Ag-CPL effectively suppresses dendrite formation and mitigates anode volume changes, thereby significantly enhancing cycling stability. Table S3 (Supporting information) summarizes the cycling performance of anode-free pouch cells with liquid electrolytes reported to date, highlighting the outstanding stability achieved in this work. To evaluate interfacial stability, electrochemical impedance spectroscopy (EIS) was conducted with fully charged cells after each cycle (Figure 5d,e). Figure S8 (Supporting information) shows the equivalent circuit for EIS analysis. As well known, the first semicircle in the high-frequency region corresponds to the film resistance (R<sub>f</sub>), while the second semicircle in the low-frequency region represents the charge-transfer resistance (R<sub>ct</sub>). Initially, the Ag-CPL-Ni cell exhibited a slightly higher interfacial resistance ( $R_i = R_f + R_{ct}$ ) due to the additional resistance introduced by the protective layer. However, the increase in interfacial resistance during subsequent cycling was significantly lower for the Ag-CPL-Ni cell compared to the bare Ni cell, clearly indicating that Ag-CPL effectively stabilizes the anode-electrolyte interface by promoting compact lithium deposition and the formation of a stable SEI. To confirm the sustained release of Ag+ ions during extended cycling, we disassembled the cell after 200

cycles. The anode was gently rinsed with 1,2-dimethoxyethane to remove loosely bound byproducts and subsequently immersed in fresh electrolyte for 24 h. ICP-MS analysis of the electrolyte detected an Ag<sup>+</sup> concentration of 419 ppm, confirming that the Ag-CPL continues to release Ag+ even after prolonged cycling. We fabricated a pouch battery by stacking 18 electrode pairs (using double-sided electrodes, 9 cathodes and 10 anodes). As shown in Figure \$9 (Supporting information), the battery initially delivered a discharge capacity of 3,090 mAh at 0.1 C (100% DoD) and demonstrated stable cycling performance at 0.5 C and 45 °C (80% DoD), retaining 96.2% of its initial capacity after 40 cycles, thereby confirming the practical applicability of Ag-CPL in multistack cells. This Ag-CPL-Ni pouch battery achieved a gravimetric energy density of 384.2 Wh kg<sup>-1</sup> and a volumetric energy density of 833.7 Wh L<sup>-1</sup>, calculated based on the cell configuration and the parameters summarized in Table S4 (Supporting information). Photographs of the single pouch cell and the stacked pouch battery are shown in Figure \$10 (Supporting information).

We investigated the effect of coating thickness on cycling performance. When the Ag-CPL thickness exceeded 2  $\mu m$ , the cells exhibited a noticeable increase in overpotential due to higher ionic resistance (Figure S11, Supporting information). Although greater thickness enhances mechanical robustness, the associated rise in resistance leads to diminished electrochemical performance. On the other hand, fabricating Ag-CPLs with a thickness below 2  $\mu m$  was very challenging. At thicknesses under 2  $\mu m$ , the coating became mechanically fragile, resulting in insufficient structural integrity and inadequate interfacial protection during cycling. This limited robustness could accelerate mechanical degradation under repeated lithium plating and stripping. Based on these results, 2  $\mu m$  was identified as the optimized thickness, offering the best balance between ionic transport and mechanical stability.

Rate capability tests further highlighted the advantages of Ag-CPL (Figure \$12a, Supporting information). The cells were charged to 4.3 V at 0.2 C rate and discharged to 3.6 V at various C rates. The cycle was repeated five times at each current rate, and the fifth discharge profiles at each C rate are shown in Figure S12b,c (Supporting information). Despite the additional resistance introduced by the cross-linked protective layer, the Ag-CPL-Ni/NCA cell exhibited comparable or higher capacities than the bare Ni/NCA cell across all current densities. Notably, at a high current rate of 3.0 C, the Ag-CPL-Ni/NCA cell delivered a specific capacity of 69.2 mAh g<sup>-1</sup>, exceeding the 63.9 mAh g<sup>-1</sup> obtained with the bare Ni cell. This enhanced performance is attributed to the polymer matrix of the Ag-CPL, which facilitates faster lithium-ion desolvation and transport, as well as the sustained release of Ag+ ions during cycling, which assists lithium nucleation and promotes uniform lithium deposition.

The morphologies of deposited lithium for fully charged Ni/NCA and Ag-CPL-Ni/NCA cells were examined using SEM analysis. The SEM images in **Figure 6**, arranged from top to bottom, depict the electrode morphologies with increasing cycle number. After the pre-conditioning cycle, the cell assembled with bare Ni exhibited a porous lithium structure (Figure 6a). In contrast, the Ag-CPL-Ni electrode showed a much denser and more uniform lithium morphology (Figure 6c), attributed to the protective layer that promotes homogeneous nucleation and growth. Furthermore, after extended cycling, the lithium metal deposited

16163028, 2025, 42, Downloaded from https://advanced.onlinelibrary.wiley.com/doi/10.1002/adfm.202518139 by Hanyang University, Wiley Online Library on [17/10/2025]. See the Terms and Conditions (https://online

on Wiley Online Library for rules

of use; OA articles are governed by the applicable Creative Commons

www.afm-journal.de

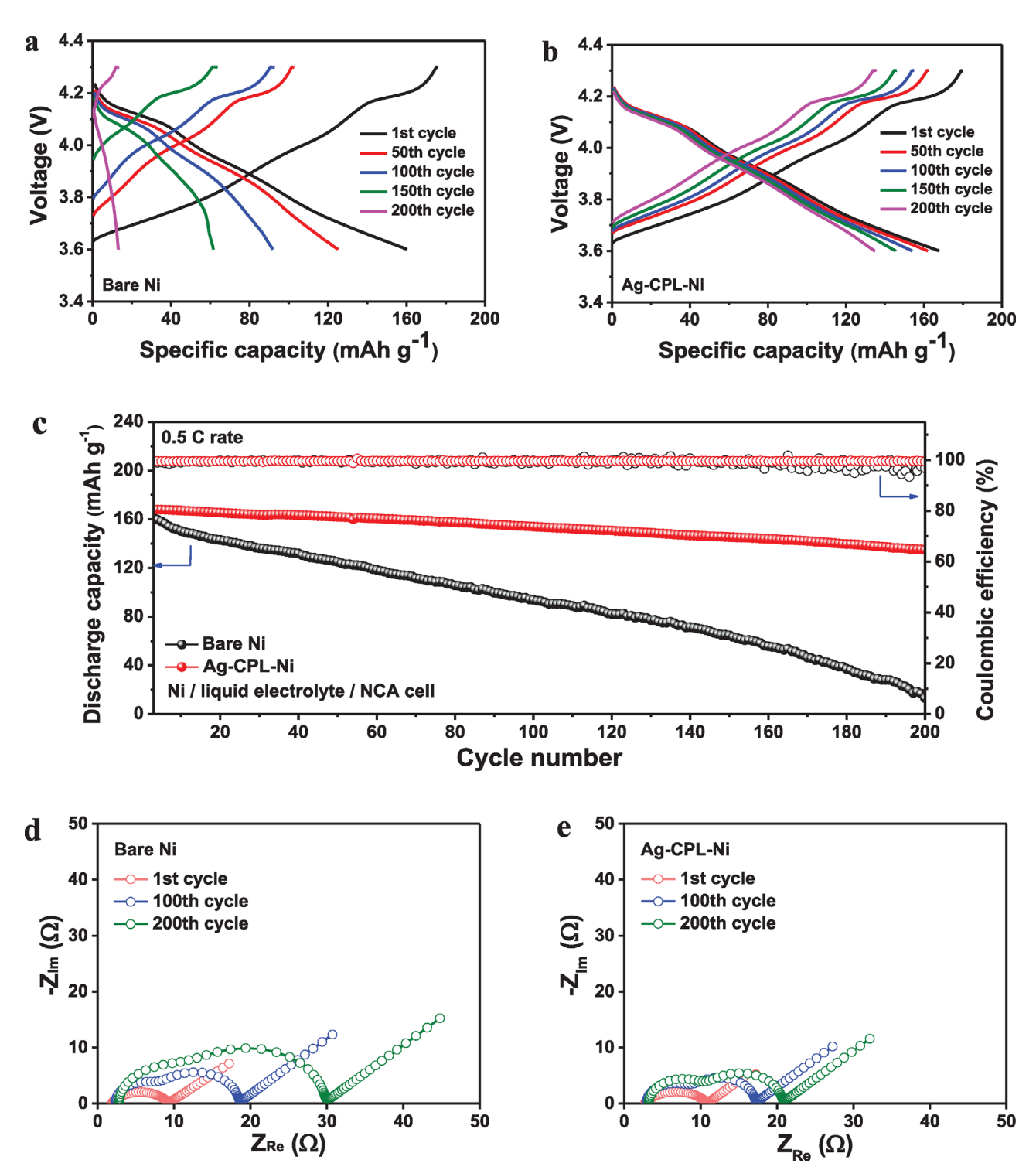


Figure 5. Voltage profiles of the Ni/NCA cells with (a) bare Ni and (b) Ag-CPL-Ni. c) Cycling performance of Ni/NCA cells with different anodes at 0.5 C rate and 45 °C. EIS plots of the Ni/NCA cells with (d) bare Ni and (e) Ag-CPL-Ni.

on bare Ni developed a mossy and dendritic morphology, indicative of irregular lithium plating/stripping caused by the intrinsic lithiophobicity of the Ni foil. In the bare Ni cell, continuous lithium plating and stripping result in the accumulation of inactive dead lithium and the formation of a highly porous lithium

structure. Consequently, the observed increase in the thickness of deposited lithium (Figure 6b) can be attributed to morphological changes, including dendrite growth and increased porosity, during cycling. Conversely, the lithium anode cycled with Ag-CPL-Ni maintained a smooth, compact, and dendrite-free surface

16163028, 2023, 42, Downloaded from https://advanced.onlinelibrary.wiley.com/doi/10.1002/adfm.202518139 by Hanyang University, Wiley Online Library on [17/10.2025]. See the Terms and Conditions (https://onlinelibrary.wiley.com/erms

and-conditions) on Wiley Online Library for rules of use; OA articles are governed by the applicable Creative Commons

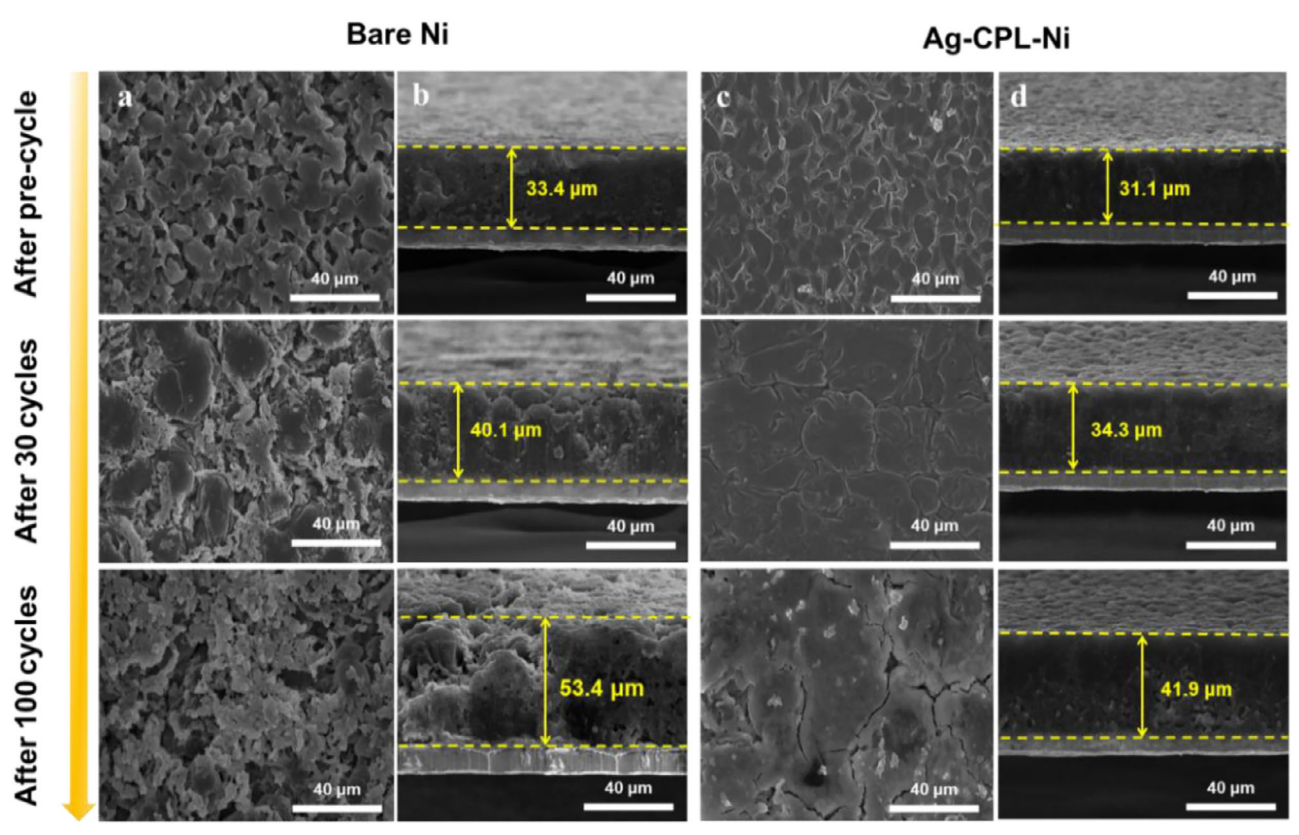


Figure 6. SEM images of deposited lithium on (a,b) bare Ni and (c,d) Ag-CPL-Ni in Ni/NCA full cells after the pre-conditioning cycle, 30 cycles, and 100 cycles. a) Top-view and (b) cross-sectional view of lithium on bare Ni. c) Top-view and (d) cross-sectional view of lithium on Ag-CPL-Ni.

morphology, which is favorable for improving cycling stability. Cross-sectional SEM images further confirm that the lithium deposited on the Ag-CPL-Ni electrode was denser, more compact, and thinner compared to that on the bare Ni electrode (Figure 6d). These observations demonstrate that the Ag-CPL protective layer effectively promotes uniform lithium deposition, thereby enhancing cycling stability and extending the lifespan of anode-free lithium metal cells.

XPS analysis was performed to investigate the chemical composition of the SEI layer formed on the lithium anode. In the F 1s spectra (Figure 7a,d), the anode cycled with Ag-CPL-Ni exhibited a notably lower intensity at 687.1 eV compared to the bare Ni anode. This peak corresponds to decomposition products of lithium salts, indicating reduced side reactions at the electrolyteanode interface due to the presence of the Ag-CPL protective layer. This conclusion is further supported by the O 1s spectra (Figure 7b,e), where distinct peaks associated with RO-Li and B-O species, originating from the decomposition of the DEC solvent and salts,[51] were more pronounced for the bare Ni electrode. Ag 3d XPS spectra provide insights into the long-term stability of AgNO<sub>3</sub> within the polymer matrix. As shown in Figure S13 (Supporting information), the surface spectra still display discernible AgNO3 peaks, indicating that AgNO3 remains chemically stable during repeated cycling. When sputtering the surface, the Ag 3d spectra reveal different chemical states. Figure 7c,f shows the deconvoluted XPS spectra of Ag 3d for the anodes cycled with bare Ni and Ag-CPL-Ni, respectively. Unlike the bare

Ni electrode, which exhibits no distinctive peaks, the Ag-CPL-Ni electrode displays peaks corresponding to metallic Ag and Ag<sub>2</sub>O. Additionally, the N 1s spectra in Figure S14 (Supporting information) reveal distinct peaks only for the lithium anode cycled with Ag-CPL-Ni, attributed to the reduction of NO<sub>3</sub><sup>-</sup>. These peaks are absent in the bare Ni electrode. The complementary TOF-SIMS maps (Figure \$15, Supporting information) further support this finding, showing specific LiN+ fragment signals exclusively for Ag-CPL-Ni. This provides straightforward confirmation of Li<sub>3</sub>N formation within the SEI, corroborating the XPS results and reinforcing the conclusion that NO<sub>3</sub><sup>-</sup> reduction enables the formation of a Li<sub>3</sub>N-enriched SEI. These results confirm that AgNO<sub>3</sub> embedded within the Ag-CPL gradually dissolves into the electrolyte during cycling and contributes to the formation of a NO<sub>3</sub><sup>-</sup>derived SEI layer on the lithium metal surface. In particular, the formation of Li<sub>3</sub>N on the lithium anode cycled with Ag-CPL-Ni enhances lithium-ion conductivity and improves the cyclability of the lithium anode. Overall, the SEM and XPS results collectively demonstrate that the incorporation of the Ag-CPL protective layer promotes uniform lithium nucleation and suppresses undesirable side reactions between the lithium anode and the electrolyte, thereby significantly enhancing the cycling stability and cycle life of AFLMBs.

Regarding the thermal stability of the Ag-CPL, we monitored the open-circuit voltage (OCV) of fully charged cells (100% SOC) at 150  $^{\circ}$ C. As shown in Figure S16 (Supporting information), the OCV of the cell with bare Ni rapidly dropped to 0 V due to

16163028, 2025, 42, Downloaded from https://adv

onlinelibrary.wiley.com/doi/10.1002/adfm.202518139 by Hanyang University, Wiley Online Library on [17/10/2025]. See the Terms and Condition

of use; OA articles are governed by the applicable Creative Commons

www.afm-journal.de

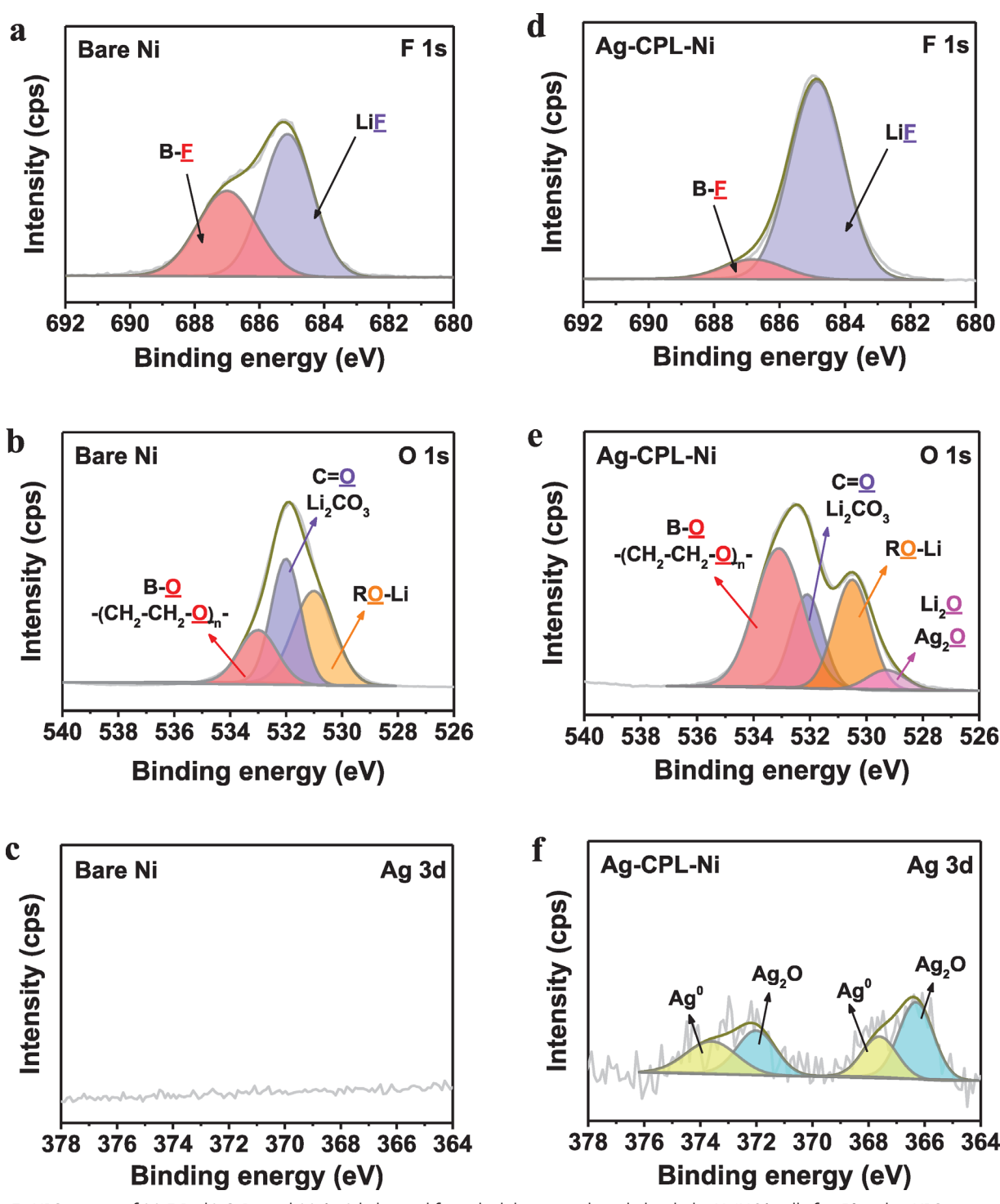


Figure 7. XPS spectra of (a) F 1s, b) O 1s, and (c) Ag 3d obtained from the lithium anode cycled with the Ni/NCA cell after 50 cycles. XPS spectra of (d) F 1s, e) O 1s, and (f) Ag 3d obtained from the lithium anode cycled with the Ag-CPL-Ni/NCA cell after 50 cycles. The Ag 3d spectra were acquired after sputtering the lithium anodes for 120 s.

thermal shrinkage of the polyolefin separator and the resulting internal short circuit. In contrast, the cell with Ag-CPL-Ni maintained stable OCV values, indicating that the Ag-CPL acted as a mechanically robust barrier that helped prevent short circuits. **Figure 8** schematically illustrates the lithium plating behavior

during the charging process with and without the Ag-CPL. As shown in Figure 8a, the conventional carbonate electrolyte without a protective layer forms a heterogeneous, organic-rich SEI, predominantly composed of ROCO<sub>2</sub>Li and ROLi. Due to the substantial volume changes of the Li anode during repeated cycling,

16163028, 2025, 42, Downloaded from https://advanced.onlinelibrary.wiley.com/doi/10.1002/adfm202518139 by Hanyang University, Wiley Online Library on [17/10.2025], See the Terms and Conditions (https://onlinelibrary.wiley.com/terms-and-conditions) on Wiley Online Library for rules of use; OA articles are governed by the applicable Creative Commons

www.afm-journal.de

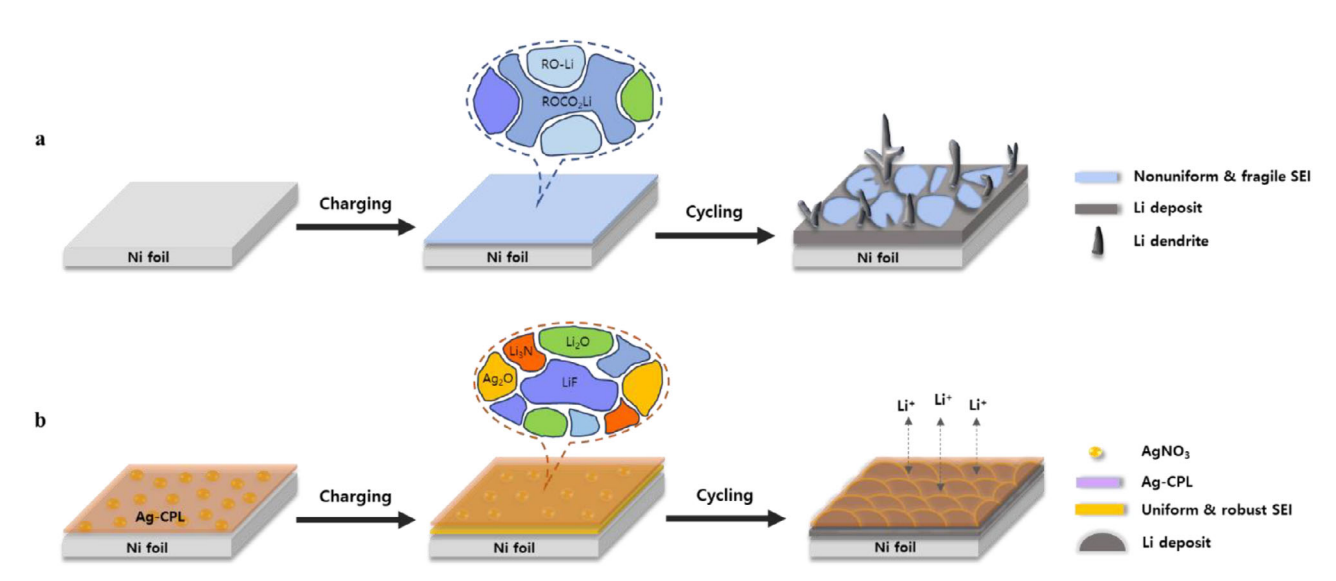


Figure 8. Schematic illustration of lithium deposition onto (a) bare Ni and (b) Ag-CPL-Ni during cycling.

this organic-rich SEI undergoes severe degradation, leading to continuous electrolyte decomposition and uneven lithium nucleation and growth. In contrast, the introduction of the Ag-CPL (Figure 8b) promotes the formation of a robust, inorganic-rich SEI, primarily consisting of  $Ag_2O$  and  $Li_3N$ , which are formed by the reduction of  $AgNO_3$  embedded within the protective layer.  $Li_3N$  exhibits high  $Li^+$  ion conductivity, while  $Ag_2O$  is converted into Li-Ag alloys during lithium plating. These characteristics collectively enable rapid and uniform lithium deposition, effectively suppressing dendrite formation and thereby enhancing the cycle life of AFLMBs.

## 3. Conclusion

In this work, we successfully introduced a silver nitratecontaining cross-linked polymer protective layer as an artificial SEI on the Ni current collector to enhance the cycling stability of AFLMBs. The cross-linked polymer layer exhibited outstanding mechanical robustness, effectively suppressing dendritic lithium growth and mitigating volume expansion during prolonged cycling. Silver nanoparticles and AgNO<sub>3</sub> embedded within the polymer matrix provided highly lithiophilic nucleation sites through the formation of Li-Ag alloys and Li<sub>3</sub>N-rich inorganic SEI components, thereby lowering the nucleation barrier and promoting uniform lithium deposition. Acrylate and fluorinated functional groups in the Ag-CPL facilitated lithium-ion desolvation and migration, leading to a higher Li+ transference number and reduced interfacial polarization. Notably, the pouch-type AFLMBs incorporating high-loading NCA cathode (active mass loading:22.5 mg cm<sup>-2</sup>, areal capacity: 4.90 mAh cm<sup>-2</sup>) and Ag-CPL-Ni demonstrated excellent capacity retention (80.4% after 200 cycles at 0.5 C) and superior rate capability compared to cells using bare Ni. Overall, this study establishes Ag-CPL as a highly effective artificial SEI layer for AFLMBs, offering valuable insights into the design of high-energy-density AFLMBs with dendrite-free lithium morphology, enhanced interfacial stability, and long-term cycling performance.

# 4. Experimental Section

*Materials*: Poly(ethylene glycol) diacrylate (PEGDA, Sigma Aldrich, average  $M_W = 700 \, g \, mol^{-1}$ ), Dipentaerythritol hexaacrylate (DPHA, TCI, purity ≥97.0%), tetra-functional perfluoropolyether (PFPE)-urethane acrylate (PFPE-UA, Fluorolink® AD1700, Solvay) were dehydrated with 4 Å molecular sieves before use. Silver nitrate (AgNO $_3$ , Alfa Aesar, purity ≥99.0%), bis(trifluoromethane) sulfonimide lithium salt (LiTFSI, Dongwha Electrolyte), tert-butyl peroxoypivalate (t-BPP, Arkema), and N, N' dimethylformamide, anhydrous (DMF, Sigma Aldrich, purity ≥99.8%) were used as received. A trilayer polypropylene-polyethylene-polypropylene (PP/PE/PP) separator (18  $\mu$ m, Celgard® S1810) was used after vacuum drying at 80 °C. The liquid electrolyte, consisting of 0.6 M LiDFOB and 0.6 M LiBF $_4$  in a DEC/FEC mixture (2:1, v/v), was provided by Dongwha Electrolyte Co., Ltd.

Preparation of the Ag-CPL-Ni: The Ag-CPL-Ni was fabricated by solution casting, as depicted in Figure S1 (Supporting information). All processes were conducted in a glovebox filled with high-purity argon gas. For the preparation of precursor solution, PEGDA, PFPE-UA, DPHA, AgNO $_3$ , and LiTFSI were dissolved in DMF at a weight ratio of 2.2: 8.7: 43.7: 36.7: 8.7, respectively, and mechanically stirred for 2 h. Additionally, 1 wt.% of t-BPP relative to the content of the cross-linking agent was added into the solution as a thermal initiator. The precursor solution was coated onto the Ni foil (10  $\mu m$ , LOTTE Energy Materials) with a doctor blade, followed by a thermal curing and drying process at 110 °C for 12 h in a vacuum oven. The resulting Ag-CPL formed on the Ni foil had a thickness of 2  $\mu m$  and contained 36.7 wt.% AgNO $_3$ , corresponding to  $\approx 0.734$  mg of AgNO $_3$ .

Electrode Preparation and Cell Assembly: The LiNi<sub>0.88</sub>Co<sub>0.10</sub>Al<sub>0.02</sub>O<sub>2</sub> (NCA) cathode was provided by Samsung SDI and coated on an aluminum current collector. The active material content was 97.7 wt.%, and its loading was ≈22.5 mg cm<sup>-2</sup>. For Ni/NCA anode-free pouch cells, the electrodes and separator were stacked and sealed with an aluminum laminated film (Youlchon Chemical). The liquid electrolyte was then injected into the cell in an amount of 6.0 g Ah<sup>-1</sup>. The Li/Ni asymmetric cells were fabricated in CR2032-type coin cells. The cells were assembled in an argonfilled glovebox using a 20 μm Li foil (Φ= 16 mm, Honjo Metal Co., Ltd.) as the counter and reference electrode, bare Ni or Ag-CPL-Ni (Φ= 18 mm) as the working electrode, a separator (Φ= 19 mm), and 12 μL of liquid electrolyte.

Electrochemical Measurements: Linear sweep voltammetry and cyclic voltammetry was performed using a potentiostat (CHI 660, CH Instruments) with the Li/Ni asymmetric cells at a scan rate of 1 mV s<sup>-1</sup>. Coulombic efficiency of the half-cells was measured by stripping the Li at the

www.afm-journal.de

16163028, 2025, 42, Downloaded from https://adv

anced.onlinelibrary.wiley.com/doi/10.1002/adfm.202518139 by Hanyang University, Wiley Online Library on [17/10/2025]. See the Terms and Conditions (https://onlinelibrary.wiley.com/erms

and-conditions) on Wiley Online Library for rules of use; OA articles are governed by the applicable Creative Commons

current density of 1 mA cm<sup>-2</sup> to a cut-off voltage of 0.5 V after galvanostatic plating of Li with a fixed capacity of 1 mAh  $\,\mathrm{cm^{-2}}$ . The cells were assembled using 20 µm Li foil as the counter/reference electrode and Ni foil (or Ag-CPL-Ni) as the working electrode. The liquid electrolyte was injected at a fixed amount of 6 g Ah<sup>-1</sup>. The galvanostatic intermittent titration technique (GITT) was conducted with Li/Li symmetric cells to evaluate Li-ion diffusion behavior. A current pulse (0.1 mA cm<sup>-2</sup> for 10 min) was applied, followed by an open-circuit rest period of 2 h, and this sequence was repeated over several cycles. The lithium-ion transference number  $(t_{Li^+})$  was calculated in the symmetric Li/electrolyte/Li cell by combining AC impedance spectroscopy and DC polarization method. Tafel curves for the electrodeposition processes of bare Ni and Ag-CPL-Ni were obtained by sweeping the voltage range from -0.2 to 0.2 V at a scan rate of 0.1mV s<sup>-1</sup>. Galvanostatic cycling tests were performed in the voltage range of 3.6-4.3 V using a battery cycler (WBCS 3000, WonATech) to evaluate the cycling performance of the pouch-type Ni/NCA cells. During the preconditioning cycle of the cell, it was charged and discharged for one cycle at 0.1 C rate. It was then charged at 0.2 C and discharged at 0.5 C in the subsequent cycles. To assess the rate capability, the cell was charged at a constant current rate of 0.2 C and discharged at current rates ranging from 0.2 to 3.0 C. Electrochemical impedance spectroscopy (EIS) of the Ni/NCA cells was conducted to measure the cell impedance over a frequency range of 1 mHz to 1 MHz at an amplitude of 5 mV using AC impedance analyzer (ZIVE MP1, WonATech Co., Ltd.). All electrochemical measurements were conducted at 45 °C.

Characterization: DFT calculation was performed using the GAMESS software with Becke's three-parameter hybrid functional combined with the Lee-Yang-Parr correlation functional (B3LYP). A field emission scanning electron microscope (FE-SEM, Verios G4UC, FEI) was used to analyze the surface morphologies of the Ag-CPL-Ni and the lithium electrodes after repeated cycling. Energy dispersive X-ray spectroscopy (EDS) was carried out to investigate the elemental distribution in the Ag-CPL coated on the Ni foil. Fourier transform infrared (FT-IR) spectroscopy was performed in the wavenumber range of 400 and 4000  $\mbox{cm}^{-1}$  to confirm the cross-linking reaction using a Nicolet iS50 spectrometer. <sup>1</sup>H NMR spectra were obtained in dimethyl sulfoxide d<sub>6</sub> (DMSO d<sub>6</sub>, Cambridge Isotope, >99.9%) with p-Xylene (Sigma Aldrich, anhydrous, ≥99%) as the reference to confirm the conversion of the cross-linking reaction using a VN-MRS 600 MHz spectrometer (Agilent Technologies). XRD patterns were obtained via MiniFlex 600 to investigate the  ${\rm AgNO_3}$  and  ${\rm Ag}$  nanoparticles in the Ag-CPL. Nanoindentation analysis of the Ag-CPL was performed under a controlled load with a maximum force of 10.0 mN using a NanoTest NTX. The chemical composition of the lithium electrode surface after the repeated cycles was investigated using X-ray photoelectron spectroscopy (XPS; K-alpha+, Thermo Fisher Scientific). Raman spectra were obtained in the range of 50–1800 cm<sup>-1</sup> using a DXR3xi Raman Imaging Microscope. The solubility of AgNO<sub>3</sub> in liquid electrolyte was determined by inductively coupled plasma-mass spectrometry (ICP-MS; iCAP RQ, Thermo Fisher Scientific).

#### Supporting Information

Supporting Information is available from the Wiley Online Library or from the author.

# Acknowledgements

A.-H.B. and J.-A.R. contributed equally to this work. This work was supported by Samsung SDI and the National Research Foundation of Korea funded by the Korean government (RS-2024-00454354).

# **Conflict of Interest**

The authors declare no conflict of interest.

# **Data Availability Statement**

The data that support the findings of this study are available from the corresponding author upon reasonable request.

# **Keywords**

3D cross-linked polymer, anode-free lithium metal battery, high energy density, in situ cross-linking, protective layer

Received: July 15, 2025 Revised: August 20, 2025 Published online: September 9, 2025

- Z. Xie, Z. Wu, X. An, X. Yue, J. Wang, A. Abudula, G. Guan, Energy Storage Mater. 2020, 32, 386.
- [2] J. B. Goodenough, K.-S. Park, J. Am. Chem. Soc. 2013, 135, 1167.
- [3] Z. P. Cano, D. Banham, S. Ye, A. Hintennach, J. Lu, M. Fowler, Z. Chen, Nat. Energy 2018, 3, 279.
- [4] J. Liu, Z. Bao, Y. Cui, E. J. Dufek, J. B. Goodenough, P. Khalifah, Q. Li, B. Y. Liaw, P. Liu, A. Manthiram, Y. S. Meng, V. R. Subramanian, M. F. Toney, V. V. Viswanathan, M. S. Whittingham, J. Xiao, W. Xu, J. Yang, X.-Q. Yang, J.-G. Zhang, Nat. Energy 2019, 4, 180.
- [5] X.-B. Cheng, R. Zhang, C.-Z. Zhao, Q. Zhang, Chem. Rev. 2017, 117, 10403.
- [6] K. Shifei, C. Jinmin, G. Weikang, C. Lifeng, Energy Mater 2023, 3, 300043.
- [7] P. Molaiyan, M. Abdollahifar, B. Boz, A. Beutl, M. Krammer, N. Zhang, A. Tron, M. Romio, M. Ricci, R. Adelung, A. Kwade, U. Lassi, A. Paolella, Adv. Funct. Mater. 2024, 34, 2311301.
- [8] S. Huo, L. Wang, B. Su, W. Xue, Y. Wang, H. Zhang, M. Li, J. Qiu, H. Xu, X. He, Adv. Mater. 2024, 36, 2411757.
- [9] J. Qian, L. Liu, J. Yang, S. Li, X. Wang, H. L. Zhuang, Y. Lu, Nat. Commun. 2018, 9, 4918.
- [10] I. T. Roe, S. K. Schnell, J. Mater. Chem. A 2021, 9, 11042.
- [11] X. Ren, L. Zou, X. Cao, M. H. Engelhard, W. Liu, S. D. Burton, H. Lee, C. Niu, B. E. Matthews, Z. Zhu, C. Wang, B. W. Arey, J. Xiao, J. Liu, J.-G. Zhang, W. Xu, *Joule* 2019, 3, 1662.
- [12] J.-N. Chazalviel, Phys. Rev. A 1990, 42, 7355.
- [13] C. Monroe, J. Newman, J. Electrochem. Soc. 2005, 152, A396.
- [14] K. Tang, L. Tian, Y. Zhang, Z. J. Xu, J. Mater. Chem. A 2024, 12, 16268
- [15] Y. Zhang, Y. Wu, H. Li, J. Chen, D. Lei, C. Wang, Nat. Commun. 2022, 13, 1297.
- [16] Z. Huang, Z. Xiao, R. Jin, Z. Li, C. Shu, R. Shi, X. Wang, Z. Tang, W. Tang, Y. Wu, Energy Environ. Sci. 2024, 17, 5365.
- [17] K. Wang, T. Zhao, R. Lv, W. Tang, T. Yu, L. Li, F. Wu, R. Chen, Adv. Funct. Mater. 2025, 08164.
- [18] W.-K. Shin, A. G. Kannan, D.-W. Kim, ACS Appl. Mater. Interfaces 2015, 7, 23700.
- [19] X. You, Y. Feng, D. Ning, H. Yao, M. Wang, J. Wang, B. Chen, G.-H. Zhong, C. Yang, W. Wu, Nano Lett. 2024, 24, 11367.
- [20] H. Kwon, J.-H. Lee, Y. Roh, J. Baek, D. J. Shin, J. K. Yoon, H. J. Ha, J. Y. Kim, H.-T. Kim, Nat. Commun. 2021, 12, 5537.
- [21] I. S. Kang, Y.-S. Lee, D.-W. Kim, J. Electrochem. Soc. 2014, 161, A53.
- [22] J. Sun, S. Zhang, J. Li, B. Xie, J. Ma, S. Dong, G. Cui, Adv. Mater. 2023, 35, 2209404.
- [23] R. Xu, X.-Q. Zhang, X.-B. Cheng, H.-J. Peng, C.-Z. Zhao, C. Yan, J.-Q. Huang, Adv. Funct. Mater. 2018, 28, 1705838.
- [24] S. M. Choi, I. S. Kang, Y.-K. Sun, J.-H. Song, S.-M. Chung, D.-W. Kim, J. Power Sources 2013, 244, 363.



www.advancedsciencenews.com



www.afm-journal.de

16163028, 2025, 42, Downloaded

from https://advanced.onlinelibrary.wiley.com/doi/10.1002/adfm.202518139 by Hanyang University, Wiley Online Library on [17/10/2025]. See the Terms

and Conditions

(https://onlinelibrary.wiley.c

and-conditions) on Wiley Online Library for rules

of use; OA articles

are governed by the applicable Creative

- [25] Y. Yu, K. Long, S. Huang, S. Yu, J. Yang, T. Naren, Y. Chen, W. Wei, X. Ji, B. Ju, G.-C. Kuang, L. Chen, Adv. Funct. Mater. 2025, 35, 2424386.
- [26] L. Chen, J. Lai, Z. Li, H. Zou, J. Yang, K. Ding, Y.-P. Cai, Q. Zheng, Commun. Mater. 2023, 4, 18.
- [27] C. Chen, J. Zhang, B. Hu, Q. Liang, X. Xiong, Nat. Commun. 2023, 14, 4018
- [28] D. Luo, L. Zheng, Z. Zhang, M. Li, Z. Chen, R. Cui, Y. Shen, G. Li, R. Feng, S. Zhang, G. Jiang, L. Chen, A. Yu, X. Wang, *Nat. Commun.* 2021, 12, 186
- [29] M. V. Ordaz, N. Pavlin, M. Gastaldi, C. Gerbaldi, R. Dominko, ACS Appl. Mater. Interfaces 2024, 16, 68237.
- [30] S. Kim, T. K. Lee, S. K. Kwak, N.-S. Choi, ACS Energy Lett. 2022, 7, 67.
- [31] C. Yang, Y. Yao, S. He, H. Xie, E. Hitz, L. Hu, Adv. Mater. 2017, 29, 1702714.
- [32] Y.-E. Park, M.-K. Oh, H.-T. Sim, H.-J. Kim, Y.-S. Cho, S.-J. Park, D.-W. Kim, ACS. Appl. Mater. Interfaces 2024, 16, 39460.
- [33] Z. Zuo, L. Zhuang, J. Xu, Y. Shi, C. Su, P. Lian, B. Tian, Front Chem 2020, 8, 109.
- [34] S. Stuckenberg, M. M. Bela, C.-T. Lechtenfeld, M. Mense, V. Kupers, T. T. K. Ingber, M. Winter, M. C. Stan, Small 2024, 20, 2305203.
- [35] C. Zhen, X. Yang, X. Wei, Y. Zhu, S. Han, X. Shi, L. Deng, M. D. Gu, Nano Lett. 2024, 24, 6714.
- [36] Y. Liu, D. Lin, Y. Li, G. Chen, A. Pei, O. Nix, Y. Li, Y. Cui, *Nat. Commun.* 2018, 9, 3656.
- [37] D.-S. Ko, S. Kim, S. Lee, G. Yoon, D. Kim, C. Shin, D. Kim, J. Lee, S. Sul, D.-J. Yun, C. Jung, Nat. Commun. 2025, 16, 1066.

- [38] M. Zhu, K. Xu, D. Li, T. Xu, W. Sun, Y. Zhu, Y. Qian, ACS Appl. Mater. Interfaces 2020, 12, 38098.
- [39] N. Stojilovic, J. Chem. Educ. 2018, 95, 598.
- [40] S. Park, B. Jeong, D.-A. Lim, C. H. Lee, K. H. Ahn, J. H. Lee, D.-W. Kim, ACS Appl. Mater. Interfaces 2020, 12, 19553.
- [41] A.-H. Ban, S.-J. Pyo, W. J. Bae, H.-S. Woo, J. Moon, D.-W. Kim, Chem. Eng. J. 2023, 475, 146266.
- [42] H. Zhou, P. Liu, Nanotechnol. 2022, 33, 112501.
- [43] Q. Cheng, T. Jin, Y. Miao, Z. Liu, J. Borovilas, H. Zhang, S. Liu, S.-Y. Kim, R. Zhang, H. Wang, X. Chen, L.-Q. Chen, J. Li, W. Min, Y. Yang, *Joule* 2022, 6, 2372.
- [44] H. Kang, T.-H. Kim, G. Hwang, G. H. Shin, J. Lee, G. Kim, E. Cho, Chem. Eng. J. 2024, 484, 149510.
- [45] S. Jin, Y. Ye, Y. Niu, Y. Xu, H. Jin, J. Wang, Z. Sun, A. Cao, X. Wu, Y. Luo, H. Ji, L. J. Wan, J. Am. Chem. Soc. 2020, 142, 8818.
- [46] T. Liu, Q. Hu, X. Li, L. Tan, G. Yan, Z. Wang, H. Guo, Y. Liu, Y. Wu, J. Wang, J. Mater. Chem. A 2019, 7, 20911.
- [47] E. S. Doyle, P. Mirmira, P. Ma, M. C. Vu, T. H. Wells, R. Kumar, C. V. Amanchukwu, Chem. Mater. 2024, 36, 5063.
- [48] X. Miao, J. Hong, S. Huang, C. Huang, Y. Liu, M. Liu, Q. Zhang, H. Jin, Adv. Funct. Mater. 2025, 35, 2411751.
- [49] K.-Y. Cho, S.-H. Hong, J. Kwon, H. Song, S. Kim, S. Jo, K. Eom, Appl. Surf. Sci. 2021, 554, 149578.
- [50] J. Li, W. Li, Y. You, A. Manthiram, Adv. Energy Mater. 2018, 8, 1801957.
- [51] C. Niu, H. Lee, S. Chen, Q. Li, J. Du, W. Xu, J.-G. Zhang, M. S. Whittingham, J. Xiao, J. Liu, Nat. Energy 2019, 4, 551.